

# NUMERICALLY EFFICIENT METHODS FOR LOW-THRUST COLLISION AVOIDANCE MANOEUVRE DESIGN

Maria Francesca Palermo<sup>(1)</sup>, Pierluigi Di Lizia<sup>(2)</sup>, and Roberto Armellin<sup>(3)</sup>

<sup>(1)</sup>Politecnico di Milano, Via La Masa 34, 20156 Milano, Italy, Email: mariafrancesca.palermo@mail.polimi.it

<sup>(2)</sup>Politecnico di Milano, Via La Masa 34, 20156 Milano, Italy, Email: pierluigi.dilizia@polimi.it

<sup>(3)</sup>Auckland Space Institute, The University of Auckland, Auckland, 1010, New Zealand. Email: roberto.armellin@auckland.ac.nz

## ABSTRACT

Critical conjunctions in space are occurring at increasing frequency due to the fast-growing and intensive use of space. Mitigating the consequent risk of collisions is of utmost importance for sustainable use of space. A further challenge is posed in the field by the recent technological advances in space propulsion: a growing number of satellites are equipped with electric propulsion systems. The problem of designing optimal low-thrust Collision Avoidance Manoeuvre (CAM) is investigated, with the aim of developing robust and numerically efficient algorithms. The conjunction dynamics is presented in Cartesian reference frame and then projected onto the B-plane, centred at the secondary object. The optimal low-thrust manoeuvre is constrained in terms of collision probability, squared Mahalanobis distance and miss distance at the time of closest approach. A fully analytical method is developed in the perspective of finding fast, reliable, and iteration-free approaches to manoeuvre design. The approach is validated in terms of efficiency and robustness in a simulated scenario accounting for environmental perturbations.

Keywords: Collision Avoidance Manoeuvres; B-plane; Low-thrust; Optimal Control Theory; Space debris.

## 1. INTRODUCTION

The ultimate purpose of providing efficient methods for Collision Avoidance Manoeuvres (CAMs) is twofold: on one hand to avoid damage to satellites, and on the other to prevent the formation of space debris.

Debris-creating events have become more common: on average over the last two decades, 12 accidental fragmentations have occurred in space every year, and this trend is unfortunately increasing. Fragmentation events describe moments in which debris is created due to collisions, explosions, electrical problems and even just the detachment of objects due to the harsh conditions in space. The estimated total number of break-ups, explosions, col-

lisions, or anomalous events resulting in fragmentation tracked by Space Surveillance Networks since the launch of the first Sputnik in 1957 is more than 560 [1]. Existing international guidelines clarify that a sustainable use of space can be achieved through the following provisions: design rockets and spacecraft to minimise the material becoming detached during launch and operation; prevent explosions by releasing stored energy; design end-of-life disposal of satellites; prevent in-space impacts through careful choice of orbits and by performing CAMs.

A collision avoidance manoeuvre is performed when, at the time of closest approach (TCA), a threshold on the miss distance (MD), or on the probability of collision (PoC), is exceeded.

Since 2009, a conjunction message has been sent by Joint Space Operations Center (JSPOC) to all spacecraft owners and operators, concerning approximately 48000 objects listed in the Two-Line Element set (TLE) provided by US Strategic Command. The standard format Conjunction Summary Message (CSM)/ Conjunction Data Message (CDM) is used for messages being prepared by the Consultative Committee for Space Data Systems (CCSDS).

ESA has implemented the Space Situation Awareness (SSA) programme, which aims to give Europe the necessary independence to acquire knowledge about the situation in space. Indeed, Europe is currently dependent on non-European information sources for its ability to monitor satellite sources of danger such as natural phenomena, Near-Earth Object (NEO) and space debris. The SSA programme focuses on Space Weather, NEOs, and Space Surveillance and Tracking (SST). Providing independent data and information, the SSA programme also enhances the reliability and availability of space. An overview of the programme can be found in [2]. SST refers to the capacity to detect, catalogue and predict the movements of space objects orbiting the Earth. The European Union established in 2014 the Space Surveillance and Tracking Support Framework, also known as the EU SST, with the Decision 541/2014/EU of the European Parliament and the Council (SST Decision).

For a typical satellite in Low Earth Orbit (LEO), hundreds of alerts are issued every week. For most of them, the

risk of collision decreases as the week goes by and more orbital information is gathered, but for some the risk is deemed high enough that further action is required. As more satellites are launched into orbit, the current standard methods for avoiding in-space collisions, and the creation of debris, will not be enough. Nowadays, CAMs are planned on-ground, with the support of specific tools. If the pre-defined threshold on the probability or on the miss distance is exceeded, a manoeuvre is designed by mission planners. The Space Debris Office (SDO) is the department of the ESA in charge of all the activities concerning space debris; a full description of the SDO current collision avoidance service can be found in [3].

From a rigorous standpoint, a collision avoidance manoeuvre is said to be optimal when it reduces the collision probability of a satellite with one, or more, space objects to a prescribed threshold while minimising a cost quantity. Most research deals with optimising impulsive manoeuvres. In order to provide a fast and efficient numerical scheme to plan last-minute and out of plane manoeuvres, Bombardelli et al. in [4], [5] and [6] studied closed-form analytic expressions and presented an efficient numerical scheme to solve the optimisation problem in its most general form. In [5] and [6], a formulation of the relative dynamics model, valid for a generic collision geometry and arbitrary eccentricity, is employed as a base for an optimisation process aimed to maximise the collision miss distance between two colliding objects for a given magnitude of available  $\Delta v$ . Then, in [4], the optimisation based on the minimisation of collision probability is also presented in case of direct and non-direct impact.

The existing literature about continuous-thrust CAM optimisation is considerably less extensive than for the impulsive case. Multi-objective particle swarm optimisers are employed by Morselli et al. [7] to design an optimal continuous-thrust CAM. Research on low-thrust optimisation methods includes the semi-analytical method developed by Reiter et al. [8] for rapid collision avoidance, based on the hypothesis that the optimal thrust is always radial. Salemme in [9] employed an indirect method formulated in Cartesian coordinates for fuel-optimal control problem (FOP) and energy-optimal control problem (EOP) solutions reaching a desired collision probability. The resulting six-dimensional optimal control problem is not easy to deal with numerically, which motivated the authors of the same paper to explore semi-analytical solutions. The dissertation of Schiavo [10] is the direct continuation of the previous study and proposes computationally efficient methods (analytical and semi-analytical) for energy optimal manoeuvres with PoC as final constraint. More semi-analytical methods were proposed in [11]; this approach is based on average dynamics and maximising the miss distance with the assumption of continuous tangential thrust. The very recent work by Bombardelli and Hernando-Ayuso [12] investigates the problem of optimum low-thrust collision avoidance between two objects in circular orbits; the thrust vector of the manoeuvred satellite, applied continuously for a given time span, is held constant in magnitude the optimal control is written in B-plane coordinates. The B-plane formulation allows to reduce significantly the dimension of the result-

ing Two-Point Boundary Value Problem (TPBVP) to only two and leads to a constant costate vector. Another recent work by Belmonte Hernandez et al. [13] presents two approaches to compute low-thrust CAM: one applies a bang-bang transformation to the EOP unbounded solution and the other formulates the manoeuvre design as a convex optimisation problem. A multi-impulse convex formulation for collision manoeuvres optimisation is also investigated in [14].

The purpose of this work is to provide robust and numerically efficient algorithms for different types of manoeuvres ultimately aiming at on-board autonomous implementability. In particular, because of the recent progress on electric propulsion technology, low-thrust manoeuvres will have an important role in space exploration and exploitation. Starting from the semi-analytical solution for the energy-optimal control problem (EOP) proposed by Schiavo in [10], a fully analytical formula is obtained; given the collision conditions and quantities in CDM format, the solution allows to design the optimal manoeuvre by substituting them directly into an analytical equation. The paper is organised as follows. In Section 2 the underlying mathematical preliminaries that are necessary to understand the methods proposed are introduced. Section 3 contains a description of the methodology developed in this work; the EOP for low-thrust CAMs is solved analytically, both exploiting the dynamics formulation in Earth Centered Inertial (ECI) reference frame and in B-plane (BP) coordinates. The performance achieved by the methods presented are analysed and compared in Section 4, leading to the conclusive Section 5.

## 2. MATHEMATICAL MODELS

This section introduces the underlying mathematical preliminaries necessary to understand the methods proposed in this work. In particular, the fundamentals of conjunction dynamics and the formulation in B-plane coordinates are first of all reported. The definition of collision probability adopted is stated right after and the derivation of the State Transition Matrix (STM) is then presented.

### 2.1. B-plane definition and collision dynamics description

Let us consider two objects experiencing a conjunction event with an expected closest approach relative position  $\mathbf{r}_e$ . We will refer to the manoeuvrable object calling it “primary”, using the symbol  $O_p$ , while the debris or uncooperative object is the “secondary” object,  $O_s$ . We define  $\mathbf{x}_p = (\mathbf{r}_p, \mathbf{v}_p)$  and  $\mathbf{x}_s = (\mathbf{r}_s, \mathbf{v}_s)$  the state vectors (position and velocity) of the center of mass of the primary and secondary objects respectively, expressed in a generic (inertial or a local) reference frame (r.f.)  $\mathfrak{R}$ . Let  $\{x, y, z\}$  represent an inertial r.f. centred at  $O_s$  at the

impact time and with axes directions defined as:

$$\mathbf{u}_x = \frac{\mathbf{v}_p}{\|\mathbf{v}_p\|}, \quad \mathbf{u}_z = \frac{\mathbf{v}_p \times \mathbf{v}_s}{\|\mathbf{v}_p \times \mathbf{v}_s\|}, \quad \mathbf{u}_y = \mathbf{u}_z \times \mathbf{u}_x. \quad (1)$$

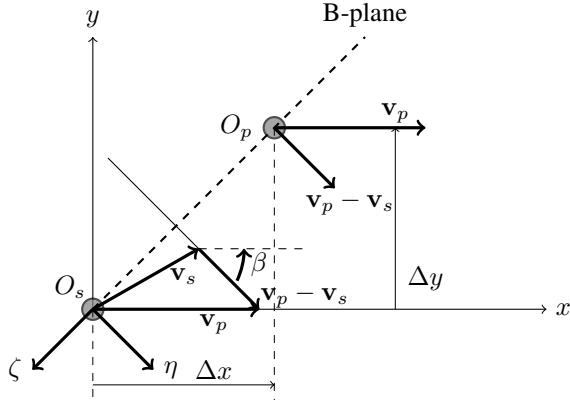


Figure 1. Encounter frame and B-plane: snapshot of  $O_p - O_s$  encounter geometry ( $x - y$  plane) after CAM.

Within a small interval of time  $\Delta t \ll 1$  around the impact event, one can consider the motion of both objects as uniform rectilinear with good approximation (hypothesis of short-term encounter, see [15]).

To describe the collision avoidance dynamics using the B-plane, the formulation of [16], centred at  $O_s$ , is adopted. The B-plane, represented in Fig. 1, is the encounter plane of the two colliding objects; it is perpendicular to their relative velocity and contains both the bodies at the moment of closest approach. We introduce the position vector  $\mathbf{b}_{3D} = [\xi, \eta, \zeta]^T$ , expressed in B-plane coordinates, defined as follows:

- $\mathbf{u}_\xi = \frac{\mathbf{v}_s \times \mathbf{v}_p}{\|\mathbf{v}_s \times \mathbf{v}_p\|}$  direction orthogonal to the geocentric velocity vectors  $\mathbf{v}_p$  and  $\mathbf{v}_s$ ;
- $\mathbf{u}_\eta = \frac{\mathbf{v}_p - \mathbf{v}_s}{\|\mathbf{v}_p - \mathbf{v}_s\|}$  direction of the velocity of  $O_p$  relative to  $O_s$ ;
- $\mathbf{u}_\zeta = \mathbf{u}_\xi \times \mathbf{u}_\eta$  direction opposite to the projection of the B-plane of the velocity of  $O_s$ .

The unit vectors define the rotation matrix from the inertial reference frame to the B-plane

$$\mathbf{R}_{b,3D} = [\mathbf{u}_\xi, \mathbf{u}_\eta, \mathbf{u}_\zeta]^T, \quad (2)$$

while the projection in the  $\eta$ -axis is achieved by

$$\mathbf{R}_{b,2D} = [\mathbf{u}_\xi, \mathbf{u}_\zeta]^T. \quad (3)$$

At TCA, the orbital elements of  $O_p$  are defined as:  $a_0$  semi-major axis,  $e_0$  eccentricity,  $R_c$  radial orbital distance,  $\theta_c$  true anomaly.

For the ease of notation, the 2D position vector in the B-plane is defined as  $\mathbf{b} = [\xi, \zeta]^T$ , constructed from the first and third components of the  $\mathbf{b}_{3D}$  vector.

The following subsections summarise the dynamics in B-plane coordinates after the derivations reported in the previous sections, and specifies the equations of motion for both the cases of impulsive manoeuvre and continuous-thrust CAM.

### 2.1.1. Impulsive manoeuvre

In case of direct impact (i.e., the position of the primary and secondary objects at TCA coincides) the position in B-plane coordinates achieved after the manoeuvre is:

$$\mathbf{b} = \mathbf{R}\mathbf{K}\mathbf{D}\Delta\mathbf{v} = \mathbf{M}\Delta\mathbf{v}, \quad (4)$$

where  $\mathbf{R}, \mathbf{K}, \mathbf{D}$  are respectively the rotation, kinetics and dynamics matrices derived in [5] and listed in Appendix A. The matrix  $\mathbf{M}$  is function of:  $\phi, \psi, \chi$  (parameters describing the transformation from  $\mathbf{v}_p$  to  $\mathbf{v}_s$ , see Appendix A),  $e_0, a_0, \theta_c$ , the Earth gravitational parameter  $\mu$  and the true anomaly  $\theta$  of the manoeuvring point.

Considering the general case of a non-direct impact (i.e., a conjunction whose expected miss distance is not zero) where  $\mathbf{b}_e$  is the relative position of the two objects at TCA in B-plane r.f.:

$$\mathbf{b}_e = \mathbf{R}_{b,2D}\mathbf{r}_e = \mathbf{R}_{b,2D}(\mathbf{r}_p - \mathbf{r}_s). \quad (5)$$

Hence the position  $\mathbf{b}$  at generic time can be written as:

$$\mathbf{b} = \mathbf{b}_e + \mathbf{M}\Delta\mathbf{v}. \quad (6)$$

### 2.1.2. Low-thrust manoeuvre

When the manoeuvrable spacecraft  $O_p$  is equipped with a low-thrust propulsion system, a realistic CAM scheme is to apply optimally oriented thrust acceleration continuously over a thrust arc. In an infinitesimal time  $\delta t$ , the control acceleration  $\mathbf{a}_c$  produces the velocity variation

$$\delta\mathbf{v} = \mathbf{a}_c\delta t. \quad (7)$$

This leads to a B-plane displacement  $\delta\mathbf{b} = [\delta\xi, \delta\zeta]^T$ :

$$\delta\mathbf{b} = \mathbf{R}\mathbf{K}\mathbf{D}\mathbf{a}_c\delta t = \mathbf{M}\mathbf{a}_c\delta t. \quad (8)$$

Approximating to the first order the Eq. 8, it is obtained:

$$\frac{d\mathbf{b}}{dt} = \mathbf{M}\mathbf{a}_c \quad (9)$$

and the dynamics of the system can be written as:

$$\begin{cases} \dot{\mathbf{b}} = \mathbf{M}\mathbf{a}_c \\ \mathbf{b}(t_0) = \mathbf{b}_e = [\xi_e, \zeta_e]^T. \end{cases} \quad (10)$$

## 2.2. Probability of collision and square Mahalanobis distance

There are several methods for calculating the 2D collision probability, many of which are collected and compared in [17]. It is chosen to follow PoC definition of Chan in [15] truncated at  $m = 3$ . The computation of PoC can be made equivalent to integrating a properly scaled isotropic Gaussian distribution function over an elliptical cross section. If the latter is approximated as a circular cross section of equal area, the final computation of the collision probability reduces to a Rician integral that can be computed with the convergent series:

$$\text{PoC}(u, v) = e^{-\frac{v}{2}} \sum_{m=0}^{\infty} \frac{v^m}{2^m m!} \left[ 1 - e^{-\frac{u}{2}} \sum_{k=0}^m \frac{u^k}{2^k k!} \right], \quad (11)$$

where  $u$  is the ratio of the impact cross-sectional area to the area of the  $1\sigma$  covariance ellipse in the B-plane:

$$u = \frac{s_A^2}{\sigma_\xi \sigma_\zeta \sqrt{1 - \rho_{\xi\zeta}^2}}, \quad (12)$$

and  $v$  is the squared Mahalanobis distance (SMD):

$$v = \text{SMD}, \quad (13)$$

$$= \left[ \left( \frac{\xi_e}{\sigma_\xi} \right)^2 + \left( \frac{\zeta_e}{\sigma_\zeta} \right)^2 - 2\rho_{\xi\zeta}^2 \frac{\xi_e \zeta_e}{\sigma_\xi \sigma_\zeta} \right] / (1 - \rho_{\xi\zeta}^2), \quad (14)$$

$$= (\mathbf{r}_f - \mathbf{r}_s)^\top \mathbf{R}_{b,2D}^\top \mathbf{C}^{-1} \mathbf{R}_{b,2D} (\mathbf{r}_f - \mathbf{r}_s), \quad (15)$$

$$= \mathbf{b}_f^\top \mathbf{C}^{-1} \mathbf{b}_f. \quad (16)$$

$\mathbf{C}$  is the combined covariance matrix in B-plane axes, which corresponds to the sum of the individual covariance matrices of the two bodies, expressed in the same orthonormal base, when the two (Gaussian) quantities are statistically independent, and then projected into 2D B-plane with components  $\{\xi, \zeta\}$ :

$$\mathbf{C} = \begin{bmatrix} \sigma_\xi^2 & \rho_{\xi\zeta} \sigma_\xi \sigma_\zeta \\ \rho_{\xi\zeta} \sigma_\xi \sigma_\zeta & \sigma_\zeta^2 \end{bmatrix}. \quad (17)$$

The miss distance is simply defined as  $d = \sqrt{\xi_e^2 + \zeta_e^2} = \|\mathbf{b}_f\| = \|\mathbf{R}_{b,2D}(\mathbf{r}_f - \mathbf{r}_s)\|$ .

## 2.3. State Transition Matrix

The State Transition Matrix (STM) maps the variation of the state  $\delta\mathbf{x}$  at an arbitrary final time  $t$  with respect to  $\delta\mathbf{x}_0$  at an arbitrary time  $t_0$ . The STM is defined as the matrix  $\Phi(t, t_0)$  such that:

$$\Phi(t, t_0) = \frac{\delta\mathbf{x}}{\delta\mathbf{x}_0}. \quad (18)$$

For time-varying systems, STM is found by integrating

$$\dot{\Phi}(t, t_0) = \mathbf{A}(t)\Phi(t, t_0), \quad \Phi(t_0, t_0) = \mathbb{I}_{n \times n}, \quad (19)$$

where  $\mathbf{A}(t)$  is the state matrix of the linear system

$$\dot{\mathbf{x}}(t) = \mathbf{A}(t)\mathbf{x}(t). \quad (20)$$

In non-linear problems such as the controlled dynamics of the Keplerian orbital motion, the goal is to linearise the equations of motion  $\mathbf{f}(\mathbf{x}, t)$  of the optimal control problem (OCP) around the nominal trajectory represented by the state  $\mathbf{x}_n$ , hence:

$$\mathbf{A}(t) = \left. \frac{\partial \mathbf{f}(\mathbf{x}, t)}{\partial \mathbf{x}} \right|_{\mathbf{x}_n}. \quad (21)$$

## 3. ENERGY-OPTIMAL CONTROL PROBLEM

This section covers the derivation of methods for optimal low-thrust CAMs exploiting the dynamics formulation in Earth-Centred Inertial (ECI) reference frame and the dynamics description in B-plane coordinates. The OCP is formulated following optimal control theory, in particular [18] is used as the main reference.

### 3.1. EOP in ECI coordinates

Let us consider the controlled motion of the primary object around Earth, considering a Keplerian orbit model. The state vector  $\mathbf{x} = [\mathbf{r}, \mathbf{v}]^\top$  consists in the position and the velocity of the satellite in ECI coordinates  $\{x, y, z\}$ . In this formulation, the mass is not included in the state variables, since its equation is decoupled from the other. Thus, to simplify the equations, it is considered separately:

$$\begin{cases} \dot{\mathbf{r}} = \mathbf{v} \\ \dot{\mathbf{v}} = -\frac{\mu}{r^3} \mathbf{r} + \mathbf{a}_c \end{cases} \quad \text{ICs} : \begin{cases} \mathbf{r}(t_0) = \mathbf{r}_0 \\ \mathbf{v}(t_0) = \mathbf{v}_0 \end{cases} \quad (22)$$

$$\dot{m} = -\frac{1}{c_e} \|\mathbf{a}_c\| m \quad \text{IC} : m(t_0) = m_0 \quad (23)$$

where  $c_e$  is the effective exhaust velocity, product of the specific impulse  $I_{sp}$  and the Earth's standard gravity acceleration  $g_0$ . In minimum-energy formulation, the control parameter is the acceleration vector  $\mathbf{a}_c = [\mathbf{a}_{c,x}, \mathbf{a}_{c,y}, \mathbf{a}_{c,z}]^\top$  and the cost function is defined as:

$$J = \int_{t_0}^{t_f} L dt, \quad L = \frac{1}{2} \mathbf{a}_c^\top \mathbf{a}_c, \quad (24)$$

and the terminal function can be written in terms of SMD (which can be translated in a PoC value, by means of Eq. 11) or MD. These two cases are discussed separately in the following subsections.

### 3.1.1. Square Mahalanobis distance constraint

The terminal function is written such that the SMD value corresponding to the final position  $\mathbf{r}_f = \mathbf{r}(t_f)$  matches with an enforced value  $\overline{\text{SMD}}$ :

$$\Psi(\mathbf{x}(t_f), t_f) = \text{SMD}(\mathbf{r}_f) - \overline{\text{SMD}} \quad (25)$$

where, from Eq. 15, using notation  $\mathbf{R}_{2D} = \mathbf{R}_{b,2D}$  for simplicity:

$$\text{SMD}(\mathbf{r}_f) = (\mathbf{r}_f - \mathbf{r}_s)^\top \mathbf{R}_{2D}^\top \mathbf{C}^{-1} \mathbf{R}_{2D} (\mathbf{r}_f - \mathbf{r}_s). \quad (26)$$

The augmented performance index is:

$$\bar{J} = \nu [\text{SMD}(\mathbf{r}_f) - \overline{\text{SMD}}] + \int_{t_0}^{t_f} \left\{ \frac{1}{2} \mathbf{a}_c^\top(t) \mathbf{a}_c(t) + \boldsymbol{\lambda}^\top(t) [\dot{\mathbf{x}}(t) - \dot{\mathbf{x}}(t)] \right\} dt, \quad (27)$$

and the Hamiltonian:

$$H = \frac{1}{2} \mathbf{a}_c^\top \mathbf{a}_c + \boldsymbol{\lambda}_r^\top \mathbf{v} + \boldsymbol{\lambda}_v^\top \left( -\frac{\mu}{r^3} \mathbf{r} + \mathbf{a}_c \right). \quad (28)$$

Exploiting optimal control theory (a complete formulation can be found in [18]), the equations of motion for the costate are derived and the Hamiltonian system associated to the EOP is:

$$\begin{cases} \dot{\mathbf{r}} = \mathbf{v} \\ \dot{\mathbf{v}} = -\frac{\mu}{r^3} \mathbf{r} + \mathbf{a}_c \\ \dot{\boldsymbol{\lambda}}_r = \frac{\mu}{r^3} \boldsymbol{\lambda}_v - \frac{3\mu \mathbf{r} \cdot \boldsymbol{\lambda}_v}{r^5} \mathbf{r} \\ \dot{\boldsymbol{\lambda}}_v = -\boldsymbol{\lambda}_r \end{cases} \quad \begin{cases} \mathbf{r}(t_0) = \mathbf{r}_0 \\ \mathbf{v}(t_0) = \mathbf{v}_0 \\ \boldsymbol{\lambda}_r(t_f) = \nu \frac{\partial \text{SMD}(\mathbf{r}_f)}{\partial \mathbf{r}_f} \\ \boldsymbol{\lambda}_v(t_f) = \nu \frac{\partial \text{SMD}(\mathbf{v}_f)}{\partial \mathbf{v}_f} \end{cases} \quad (29)$$

with the control acceleration law deriving from the Pontryagin's minimum principle which states that the optimal control is the one that minimises the Hamiltonian:

$$\mathbf{a}_c = -\boldsymbol{\lambda}_v. \quad (30)$$

The problem can be formulated as a TPBVP (known as Euler-Lagrange equations):

$$\begin{cases} \dot{\mathbf{r}} = \mathbf{v} \\ \dot{\mathbf{v}} = -\frac{\mu}{r^3} \mathbf{r} - \boldsymbol{\lambda}_v \\ \dot{\boldsymbol{\lambda}}_r = \frac{\mu}{r^3} \boldsymbol{\lambda}_v - \frac{3\mu \mathbf{r} \cdot \boldsymbol{\lambda}_v}{r^5} \mathbf{r} \\ \dot{\boldsymbol{\lambda}}_v = -\boldsymbol{\lambda}_r \end{cases} \quad (31)$$

$$\text{BCs} : \begin{cases} \mathbf{r}(t_0) = \mathbf{r}_0 \\ \mathbf{v}(t_0) = \mathbf{v}_0 \\ \boldsymbol{\lambda}_r(t_f) = \nu 2\mathbf{R}_{2D}^\top \mathbf{C}^{-1} \mathbf{R}_{2D} (\mathbf{r}_f - \mathbf{r}_s) \\ \boldsymbol{\lambda}_v(t_f) = 0 \end{cases} \quad (32)$$

with a constraint on the final square Mahalanobis distance:

$$\text{SMD}(\mathbf{r}_f) - \overline{\text{SMD}} = 0. \quad (33)$$

Several numerical techniques exist for solving TPBVPs, usually iterative and time-consuming methods where the convergence depends on the first guess. In this research the problem is solved in a completely analytical way avoiding numerical methods, and the procedure is described in detail hereafter. The purpose is to determine the initial costates  $\boldsymbol{\lambda}_{r0}, \boldsymbol{\lambda}_{v0}$  to transform the problem into an Initial Value Problem (IVP). The STM and the equation of the final constraint are exploited to achieve this goal.

$$\begin{cases} \dot{\mathbf{r}} = \mathbf{v} \\ \dot{\mathbf{v}} = -\frac{\mu}{r^3} \mathbf{r} - \boldsymbol{\lambda}_v \\ \dot{\boldsymbol{\lambda}}_r = \frac{\mu}{r^3} \boldsymbol{\lambda}_v - \frac{3\mu \mathbf{r} \cdot \boldsymbol{\lambda}_v}{r^5} \mathbf{r} \\ \dot{\boldsymbol{\lambda}}_v = -\boldsymbol{\lambda}_r \end{cases} \quad \text{ICs} : \begin{cases} \mathbf{r}(t_0) = \mathbf{r}_0 \\ \mathbf{v}(t_0) = \mathbf{v}_0 \\ \boldsymbol{\lambda}_r(t_0) = \boldsymbol{\lambda}_{r0} \\ \boldsymbol{\lambda}_v(t_0) = \boldsymbol{\lambda}_{v0}. \end{cases} \quad (34)$$

Once the IVP is obtained, it can be solved for the state variables  $[\mathbf{r}, \mathbf{v}]$  and the costates  $[\boldsymbol{\lambda}_r, \boldsymbol{\lambda}_v]$ . The control acceleration profile of the optimal manoeuvre can be simply found by substituting the velocity costate into the control law in Eq. 30.

To find the initial costates, the deviations of the spacecraft from the nominal trajectory are linearised using the STM. The nominal ballistic trajectory consists in the natural motion of the satellite around the Earth:

$$\begin{cases} \dot{\mathbf{r}}_n = \mathbf{v}_n \\ \dot{\mathbf{v}}_n = -\frac{\mu}{r^3} \mathbf{r} \\ \dot{\boldsymbol{\lambda}}_{rn} = \mathbf{0} \\ \dot{\boldsymbol{\lambda}}_{vn} = \mathbf{0}. \end{cases} \quad (35)$$

Expanding the dynamics in Eq. 34 about the ballistic solution Eq. 35, the state matrix  $\mathbf{A}$  can be computed from Eq. 21 and reads:

$$\mathbf{A} = \begin{bmatrix} \mathbf{0}_{3 \times 3} & \mathbb{I}_{3 \times 3} & \mathbf{0}_{3 \times 3} & \mathbf{0}_{3 \times 3} \\ -\mathbf{A}_{34} & \mathbf{0}_{3 \times 3} & \mathbf{0}_{3 \times 3} & -\mathbb{I}_{3 \times 3} \\ \mathbf{0}_{3 \times 3} & \mathbf{0}_{3 \times 3} & \mathbf{0}_{3 \times 3} & \mathbf{A}_{34} \\ \mathbf{0}_{3 \times 3} & \mathbf{0}_{3 \times 3} & -\mathbb{I}_{3 \times 3} & \mathbf{0}_{3 \times 3} \end{bmatrix} \quad (36)$$

where

$$\mathbf{A}_{34} = \frac{\mu}{r_n^3} \mathbb{I}_{3 \times 3} - 3 \frac{\mu}{r_n^5} \begin{bmatrix} \mathbf{r}_n(x)^2 & \mathbf{r}_n(y)\mathbf{r}_n(x) & \mathbf{r}_n(z)\mathbf{r}_n(x) \\ \mathbf{r}_n(x)\mathbf{r}_n(y) & \mathbf{r}_n(y)^2 & \mathbf{r}_n(z)\mathbf{r}_n(y) \\ \mathbf{r}_n(x)\mathbf{r}_n(z) & \mathbf{r}_n(y)\mathbf{r}_n(z) & \mathbf{r}_n(z)^2 \end{bmatrix}. \quad (37)$$

Here,  $\mathbf{r}_n(x)$ ,  $\mathbf{r}_n(y)$  and  $\mathbf{r}_n(z)$  are the components of the position vector on the nominal orbit  $\mathbf{r}_n$ , expressed in ECI. Using the STM, computed by integrating Eq. 19, the variations of the initial states are then linearly mapped into variations of the final state:

$$\begin{bmatrix} \delta \mathbf{r}_f \\ \delta \mathbf{v}_f \\ \delta \boldsymbol{\lambda}_{rf} \\ \delta \boldsymbol{\lambda}_{vf} \end{bmatrix} = \begin{bmatrix} \Phi_{11} & \Phi_{12} & \Phi_{13} & \Phi_{14} \\ \Phi_{21} & \Phi_{22} & \Phi_{23} & \Phi_{24} \\ \Phi_{31} & \Phi_{32} & \Phi_{33} & \Phi_{34} \\ \Phi_{41} & \Phi_{42} & \Phi_{43} & \Phi_{44} \end{bmatrix} \begin{bmatrix} \delta \mathbf{r}_0 \\ \delta \mathbf{v}_0 \\ \delta \boldsymbol{\lambda}_{r0} \\ \delta \boldsymbol{\lambda}_{v0} \end{bmatrix}. \quad (38)$$

In this approach the initial state is fixed, hence  $\delta \mathbf{r}_0 = \mathbf{0}$ ,  $\delta \mathbf{v}_0 = \mathbf{0}$  and the costates are zero on the nominal trajectory (see Eq. 35), therefore:  $\delta \lambda_{r_0} = \lambda_{r_0}$ ,  $\delta \lambda_{v_0} = \lambda_{v_0}$ . The variations of state and costate at the time of closest approach after the manoeuvre are:

$$\delta \mathbf{r}_f = \mathbf{r}_f - \mathbf{r}_p, \quad (39)$$

$$\delta \mathbf{v}_f = \mathbf{v}_f - \mathbf{v}_p. \quad (40)$$

The equations derived from the STM are now used to express the initial costates  $\lambda_{r_0}$ ,  $\lambda_{v_0}$  as a functions of the final position  $\mathbf{r}_f$ .

Since the final velocity is free, the associated costate is zero:  $\delta \lambda_{v_f} = \lambda_{v_f} = \mathbf{0}$ . Thus, from the fourth row of Eq. 38, it can be derived:

$$0 = \Phi_{43} \delta \lambda_{r_0} + \Phi_{44} \delta \lambda_{v_0}, \quad (41)$$

and from the third row of Eq. 38:

$$\begin{aligned} \delta \lambda_{r_f} &= \Phi_{33} \delta \lambda_{r_0} + \Phi_{34} \delta \lambda_{v_0} \\ &= (\Phi_{33} - \Phi_{34} \Phi_{44}^{-1} \Phi_{43}) \delta \lambda_{r_0} \\ &= \mathbf{B} \delta \lambda_{r_0} \\ &\rightarrow \lambda_{r_0} = \mathbf{B}^{-1} \delta \lambda_{r_f}. \end{aligned} \quad (42)$$

Considering now the first row of Eq. 38:

$$\begin{aligned} \delta \mathbf{r}_f &= \Phi_{13} \delta \lambda_{r_0} + \Phi_{14} \delta \lambda_{v_0} \\ &= (\Phi_{13} - \Phi_{14} \Phi_{44}^{-1} \Phi_{43}) \delta \lambda_{r_0} \\ &= \mathbf{D} \delta \lambda_{r_0} \\ &= \mathbf{D} \mathbf{B}^{-1} \delta \lambda_{r_f} \end{aligned} \quad (43)$$

$$\mathbf{B} = \Phi_{33} - \Phi_{34} \Phi_{44}^{-1} \Phi_{43} \quad (44)$$

$$\mathbf{D} = \Phi_{13} - \Phi_{14} \Phi_{44}^{-1} \Phi_{43}. \quad (45)$$

Recalling now that  $\delta \lambda_{r_f} = \lambda_{r_f}$ ,

$$\delta \mathbf{r}_f = \mathbf{D} \mathbf{B}^{-1} \lambda_{r_f} = \mathbf{D} \mathbf{B}^{-1} \nu \frac{\partial \text{SMD}(\mathbf{r}_f)}{\partial \mathbf{r}_f} \quad (46)$$

Hence the variation of the position vector can be written as the product of the multiplier  $\nu$  and a function  $\mathbf{g}$  of the final position  $\mathbf{r}_f$ :

$$\delta \mathbf{r}_f = \nu \mathbf{g}(\mathbf{r}_f) \quad (47)$$

where, computing the derivation of the squared Mahalanobis distance from Eq. 26:

$$\mathbf{g}(\mathbf{r}_f) = 2 \mathbf{D} \mathbf{B}^{-1} \mathbf{R}_{2D}^{\top} \mathbf{C}^{-1} \mathbf{R}_{2D} (\mathbf{r}_f - \mathbf{r}_s). \quad (48)$$

A non-linear system in  $\mathbf{r}_f$  and  $\nu$  is obtained from Eq. 47 and Eq. 33:

$$\begin{cases} \delta \mathbf{r}_f = \mathbf{r}_f - \mathbf{r}_p = \nu \mathbf{g}(\mathbf{r}_f) \\ \text{SMD}(\mathbf{r}_f) = \overline{\text{SMD}}. \end{cases} \quad (49)$$

By means of Eq. 26, Eq. 39 and Eq. 48, the non-linear system in Eq. 49 can be rewritten as:

$$\begin{cases} \mathbf{r}_f - \mathbf{r}_p = 2 \nu \mathbf{D} \mathbf{B}^{-1} \mathbf{R}_{2D}^{\top} \mathbf{C}^{-1} \mathbf{R}_{2D} (\mathbf{r}_f - \mathbf{r}_s) \\ (\mathbf{r}_f - \mathbf{r}_s)^{\top} \mathbf{R}_{2D}^{\top} \mathbf{C}^{-1} \mathbf{R}_{2D} (\mathbf{r}_f - \mathbf{r}_s) = \overline{\text{SMD}}, \end{cases} \quad (50)$$

recalling that  $\mathbf{r}_p, \mathbf{r}_s$  are respectively the position of the primary and the secondary object at TCA,  $\mathbf{C}$  is the 2D combined covariance matrix in BP coordinates and  $\mathbf{R}_{2D}$  is the rotation matrix from ECI r.f. to BP r.f.

The first equation of Eq. 50 is multiplied to the left by  $\mathbf{R}_{2D}$  and the second one is rewritten in terms of final position  $\mathbf{b}_f$  in B-plane (Eq. 16):

$$\begin{cases} \mathbf{R}_{2D} (\mathbf{r}_f - \mathbf{r}_p) = 2 \nu \mathbf{R}_{2D} \mathbf{D} \mathbf{B}^{-1} \mathbf{R}_{2D}^{\top} \mathbf{C}^{-1} \mathbf{R}_{2D} (\mathbf{r}_f - \mathbf{r}_s) \\ \mathbf{b}_f^{\top} \mathbf{C}^{-1} \mathbf{b}_f = \overline{\text{SMD}}. \end{cases} \quad (51)$$

Focusing on the first equation of Eq. 51, recalling that a generic position  $\mathbf{b}$  in BP coordinates can be written as  $\mathbf{b} = \mathbf{R}_{2D} (\mathbf{r} - \mathbf{r}_s)$ :

$$\begin{aligned} \mathbf{R}_{2D} (\mathbf{r}_f - \mathbf{r}_s - \mathbf{r}_p + \mathbf{r}_s) &= \\ 2 \nu \mathbf{R}_{2D} \mathbf{D} \mathbf{B}^{-1} \mathbf{R}_{2D}^{\top} \mathbf{C}^{-1} \mathbf{R}_{2D} (\mathbf{r}_f - \mathbf{r}_s) \end{aligned} \quad (52)$$

$$\mathbf{b}_f - \mathbf{b}_p = 2 \nu \mathbf{R}_{2D} \mathbf{D} \mathbf{B}^{-1} \mathbf{R}_{2D}^{\top} \mathbf{C}^{-1} \mathbf{b}_f. \quad (53)$$

Let us define the matrix  $\mathbf{E} = 2 \mathbf{R}_{2D} \mathbf{D} \mathbf{B}^{-1} \mathbf{R}_{2D}^{\top} \mathbf{C}^{-1}$ . Eq. 53 becomes:

$$\mathbf{b}_f = (\mathbb{I}_{2 \times 2} - \nu \mathbf{E})^{-1} \mathbf{b}_p. \quad (54)$$

By substituting Eq. 54 into the second equation of Eq. 51, the latter can be written as a scalar equation with unknown  $\nu$ . Setting the matrix  $\mathbf{Q} = \mathbf{C}^{-1}$ , it reads:

$$[(\mathbb{I}_{2 \times 2} - \nu \mathbf{E})^{-1} \mathbf{b}_p]^{\top} \mathbf{Q} (\mathbb{I}_{2 \times 2} - \nu \mathbf{E})^{-1} \mathbf{b}_p = \overline{\text{SMD}}. \quad (55)$$

Since:

$$(\mathbb{I} - \nu \mathbf{E})^{-1} = \frac{1}{\det(\mathbb{I} - \nu \mathbf{E})} [\mathbb{I} - \nu \det \mathbf{E} \cdot (\mathbf{E})^{-1}] \quad (56)$$

Equation 55 becomes:

$$\frac{1}{\det^2(\mathbb{I} - \nu \mathbf{E})} [(\mathbb{I} - \nu \det \mathbf{E} \cdot \mathbf{E}^{-1}) \mathbf{b}_p]^{\top} \mathbf{Q} (\mathbb{I} - \nu \det \mathbf{E} \cdot \mathbf{E}^{-1}) \mathbf{b}_p = \overline{\text{SMD}}. \quad (57)$$

Let us introduce also the matrix  $\tilde{\mathbf{E}} = \det \mathbf{E} \cdot \mathbf{E}^{-1}$  in order to simplify the notation. Equation 57, through simple algebraic steps, is written as:

$$[(\mathbb{I} - \nu \tilde{\mathbf{E}}) \mathbf{b}_p]^{\top} \mathbf{Q} (\mathbb{I} - \nu \tilde{\mathbf{E}}) \mathbf{b}_p = \overline{\text{SMD}} \det^2(\mathbb{I} - \nu \mathbf{E}) \quad (58)$$

$$[\mathbf{b}_p^{\top} - \nu (\tilde{\mathbf{E}} \mathbf{b}_p)^{\top}] \mathbf{Q} [\mathbf{b}_p - \nu \tilde{\mathbf{E}} \mathbf{b}_p] = \overline{\text{SMD}} \det^2(\mathbb{I} - \nu \mathbf{E}) \quad (59)$$

$$\begin{aligned} \mathbf{b}_p^{\top} \mathbf{Q} \mathbf{b}_p - \nu \mathbf{b}_p^{\top} \mathbf{Q} \tilde{\mathbf{E}} \mathbf{b}_p - \nu (\tilde{\mathbf{E}} \mathbf{b}_p)^{\top} \mathbf{Q} \mathbf{b}_p + \\ \nu^2 (\tilde{\mathbf{E}} \mathbf{b}_p)^{\top} \mathbf{Q} (\tilde{\mathbf{E}} \mathbf{b}_p) = \overline{\text{SMD}} \det^2(\mathbb{I} - \nu \mathbf{E}). \end{aligned} \quad (60)$$

The analytical equation is finally written in the normal polynomial form and can be solved in a closed-form for  $\nu$ :

$$\begin{aligned} \nu^2 (\tilde{\mathbf{E}} \mathbf{b}_p)^{\top} \mathbf{Q} (\tilde{\mathbf{E}} \mathbf{b}_p) - \nu [\mathbf{b}_p^{\top} \mathbf{Q} \tilde{\mathbf{E}} \mathbf{b}_p + (\tilde{\mathbf{E}} \mathbf{b}_p)^{\top} \mathbf{Q} \mathbf{b}_p] = \\ \overline{\text{SMD}} \det^2(\mathbb{I} - \nu \mathbf{E}) - \mathbf{b}_p^{\top} \mathbf{Q} \mathbf{b}_p. \end{aligned} \quad (61)$$

Equation 61 has four solutions, since the term with the quadratic determinant contains  $\nu$  at the fourth degree. The solutions corresponds to the two local minima and two local maxima in terms of equivalent  $\Delta v$  (as it is shown in the results section, Fig. 8).

The final position reached after the manoeuvre  $\mathbf{r}_f$  can be found by plugging the solution  $\nu$  into the first equation of Eq. 50. Once  $\mathbf{r}_f$  is known, recalling that  $\delta\mathbf{r}_f = \mathbf{r}_f - \mathbf{r}_p$ , it is finally possible to compute the initial costates  $\lambda_{v0}$  and  $\lambda_{v0}$  from Eqs. 41 and 43:

$$\lambda_{r0} = \mathbf{D}^{-1}\delta\mathbf{r}_f, \quad (62)$$

$$\lambda_{v0} = -\Phi_{44}^{-1}\Phi_{43}\delta\mathbf{r}_0. \quad (63)$$

The IVP in Eq. 34, given all the initial conditions, can now be integrated.

### 3.1.2. Miss distance constraint

The EOP manoeuvre can be reformulated considering a constraint not on the final PoC/SMD but on the final MD value. Remember that the miss distance  $d$  can be written as:  $d = \sqrt{\xi_e^2 + \zeta_e^2} = \|\mathbf{b}_f\| = \|\mathbf{R}_{2D}(\mathbf{r}_f - \mathbf{r}_s)\|$ . The non-linear system in Eq. 49 becomes:

$$\begin{cases} \delta\mathbf{r}_f = 2\nu\mathbf{D}\mathbf{B}^{-1}\mathbf{R}_{2D}^\top\mathbf{C}^{-1}\mathbf{R}_{2D}(\mathbf{r}_f - \mathbf{r}_s) \\ d(\mathbf{r}_f) = \bar{d}, \end{cases} \quad (64)$$

$$\begin{cases} \mathbf{R}_{2D}(\mathbf{r}_f - \mathbf{r}_p) = 2\nu\mathbf{R}_{2D}\mathbf{D}\mathbf{B}^{-1}\mathbf{R}_{2D}^\top\mathbf{C}^{-1}\mathbf{R}_{2D}(\mathbf{r}_f - \mathbf{r}_s) \\ \|\mathbf{R}_{2D}(\mathbf{r}_f - \mathbf{r}_s)\| = \bar{d}. \end{cases} \quad (65)$$

One can apply the same procedure of the previous paragraph (Eqs. 52 - 54), and the first equation of Eq. 65 reads:

$$\mathbf{b}_f = (\mathbb{I}_{2 \times 2} - \nu\mathbf{E})^{-1}\mathbf{b}_p. \quad (66)$$

The second equation of Eq. 65 becomes:

$$\|(\mathbb{I} - \nu\mathbf{E})^{-1}\mathbf{b}_p\| = \bar{d}, \quad (67)$$

and similarly to Eqs. 56 - 58:

$$\left\| \frac{1}{\det(\mathbb{I} - \nu\mathbf{E})}(\mathbb{I} - \nu\tilde{\mathbf{E}})\mathbf{b}_p \right\| = \bar{d}. \quad (68)$$

$$\nu^2(\tilde{\mathbf{E}}\mathbf{b}_p)^\top(\tilde{\mathbf{E}}\mathbf{b}_p) - \nu\mathbf{b}_p^\top(\tilde{\mathbf{E}}\mathbf{b}_p) - \nu(\tilde{\mathbf{E}}\mathbf{b}_p)^\top\mathbf{b}_p = \det(\mathbb{I} - \nu\mathbf{E})^2\bar{d}^2 - \mathbf{b}_p^\top\mathbf{b}_p \quad (69)$$

In analogy to what has been explained for the SMD case, Eq. 68 is algebraically manipulated and analytically solved for  $\nu$  and used to find the initial costates and integrate the IVP.

## 3.2. EOP in B-plane coordinates

The EOP formulation can be projected onto the B-Plane and the resulting approach simplifies the problem by reducing the dimension of the system from six to two. The detailed derivation of the conjunction dynamics expressed in B-plane coordinated can be found in [12]. The state vector in B-plane coordinates  $\{\xi, \zeta\}$  is  $\mathbf{b} = [b_\xi, b_\zeta]^\top$ . The control parameter is the acceleration, expressed in ECI r.f.:  $\mathbf{a}_c = [\mathbf{a}_{c,x}, \mathbf{a}_{c,y}, \mathbf{a}_{c,z}]^\top$ . The dynamic system can be written as:

$$\begin{cases} \dot{\mathbf{b}} = \mathbf{M}\mathbf{a}_c \\ \text{IC} : \mathbf{b}(t_0) = \mathbf{b}_0. \end{cases} \quad (70)$$

recall the definition of the matrix  $\mathbf{M}$  as the product of the three matrices that describe the rotation, kinematics and dynamics from ECI r.f. to the B-plane:

$$\mathbf{M}(t) = \mathbf{R}\mathbf{K}\mathbf{D}(t). \quad (71)$$

The performance index is:

$$L = \frac{1}{2}\mathbf{a}_c^\top\mathbf{a}_c \quad (72)$$

and as in Cartesian coordinates, the terminal function can be written in terms of SMD (which includes also the PoC case) or MD.

### 3.2.1. Squared Mahalanobis distance constraint

The problem is constrained such that the final SMD value matches with an enforced value SMD. Thus the terminal function can be written as:

$$\Psi(\mathbf{x}(t_f), t_f) = \mathbf{b}^\top(t_f)\mathbf{C}^{-1}\mathbf{b}(t_f) - \overline{\text{SMD}}. \quad (73)$$

The augmented cost function is:

$$\begin{aligned} \bar{J} = & \nu [\mathbf{b}^\top(t_f)\mathbf{C}^{-1}\mathbf{b}(t_f) - \overline{\text{SMD}}] + \\ & + \int_{t_0}^{t_f} \left\{ \frac{1}{2}\mathbf{a}_c^\top(t)\mathbf{a}_c(t) + \boldsymbol{\lambda}^\top(t) [\mathbf{M}(t)\mathbf{a}_c(t) - \dot{\mathbf{b}}(t)] \right\} dt \end{aligned} \quad (74)$$

and the Hamiltonian reads:

$$H = \frac{1}{2}\mathbf{a}_c^\top\mathbf{a}_c + \boldsymbol{\lambda}^\top\mathbf{M}\mathbf{a}_c. \quad (75)$$

The Hamiltonian system associated to the EOP results to be:

$$\begin{cases} \dot{\mathbf{b}} = \mathbf{M}\mathbf{a}_c \\ \dot{\boldsymbol{\lambda}} = \mathbf{0} \\ \mathbf{b}(t_0) = \mathbf{b}_0 \\ \boldsymbol{\lambda}(t_f) = \nu 2\mathbf{C}^{-1}\mathbf{b}(t_f) \\ \mathbf{a}_c = -\mathbf{M}^\top\boldsymbol{\lambda}. \end{cases} \quad (76)$$

By substituting the resulting definition of the control acceleration  $\mathbf{a}_c$  as function of the costate  $\boldsymbol{\lambda}$  into the dynamics, the TPBVP can be written as:

$$\begin{cases} \dot{\mathbf{b}} = -\mathbf{M}(t)\mathbf{M}^\top(t)\boldsymbol{\lambda} \\ \dot{\boldsymbol{\lambda}} = \mathbf{0} \end{cases} \quad \text{BCs: } \begin{cases} \mathbf{b}(t_0) = \mathbf{b}_0 \\ \boldsymbol{\lambda}(t_f) = \nu 2\mathbf{C}^{-1}\mathbf{b}(t_f) \end{cases} \quad (77)$$

with the constraint on the final squared Mahalanobis distance

$$\mathbf{b}^\top(t_f)\mathbf{C}^{-1}\mathbf{b}(t_f) - \overline{\text{SMD}} = 0. \quad (78)$$

Since the Hamiltonian does not explicitly depend on the  $\mathbf{b}$  vector coordinates,  $\boldsymbol{\lambda}$  remains constant in time:

$$\boldsymbol{\lambda}(t_0) = \boldsymbol{\lambda}(t) = \nu 2\mathbf{C}^{-1}\mathbf{b}(t_f), \quad \forall t \in (t_0, t_f) \quad (79)$$

As explained in Section 3.1, relative to the Cartesian formulation of the problem, also in this case the TPBVP can be translated into a IVP after  $\boldsymbol{\lambda}_0$  is known. Equation 79 already links  $\boldsymbol{\lambda}$  to the final position  $\mathbf{b}_f$ , thus  $\mathbf{b}_f$  needs to be estimated using the STM and the constraint in Eq. 78 in order to formulate the initial conditions for an IVP:

$$\begin{cases} \dot{\mathbf{b}} = -\mathbf{M}(t)\mathbf{M}^\top(t)\boldsymbol{\lambda} \\ \dot{\boldsymbol{\lambda}} = \mathbf{0} \end{cases} \quad \text{ICs: } \begin{cases} \mathbf{b}(t_0) = \mathbf{b}_0 \\ \boldsymbol{\lambda}(t) = \boldsymbol{\lambda}_0. \end{cases} \quad (80)$$

The natural motion of the satellite around the Earth expressed in B-plane dynamics is expressed by means of Eq. 8:

$$\begin{cases} \dot{\mathbf{b}}_n = -\mathbf{M}\mathbf{M}^\top\boldsymbol{\lambda}_n \\ \dot{\boldsymbol{\lambda}}_n = \mathbf{0}. \end{cases} \quad (81)$$

The State Transition Matrix is computed by integrating:

$$\dot{\boldsymbol{\Phi}}(t, t_0) = \mathbf{A}(t)\boldsymbol{\Phi}(t_0, t_0), \quad \boldsymbol{\Phi}(t_0, t_0) = \mathbb{I}_{4 \times 4} \quad (82)$$

where  $\mathbf{A}(t)$  is the state matrix of the linear system

$$\dot{\mathbf{x}}(t) = \mathbf{A}(t)\mathbf{x}(t). \quad (83)$$

For this formulation of the problem it can be written as:

$$\mathbf{A} = \begin{bmatrix} \mathbf{0}_{2 \times 2} & -\mathbf{M}\mathbf{M}^\top \\ \mathbf{0}_{2 \times 2} & \mathbf{0}_{2 \times 2} \end{bmatrix}, \quad \text{such that: } \begin{bmatrix} \dot{\mathbf{b}} \\ \dot{\boldsymbol{\lambda}} \end{bmatrix} = \mathbf{A} \begin{bmatrix} \mathbf{b} \\ \boldsymbol{\lambda} \end{bmatrix}. \quad (84)$$

Hence the STM turns out to be:

$$\begin{bmatrix} \delta\mathbf{b}_f \\ \delta\boldsymbol{\lambda}_f \end{bmatrix} = \begin{bmatrix} \boldsymbol{\Phi}_{11} & \boldsymbol{\Phi}_{12} \\ \boldsymbol{\Phi}_{21} & \boldsymbol{\Phi}_{22} \end{bmatrix} \begin{bmatrix} \delta\mathbf{b}_0 \\ \delta\boldsymbol{\lambda}_0 \end{bmatrix}. \quad (85)$$

Considering that the initial state is fixed  $\delta\mathbf{b}_0 = \mathbf{0}$  and the costate is zero on the nominal trajectory (see Eq. 81),  $\delta\boldsymbol{\lambda}_0 = \boldsymbol{\lambda}_0$ , the variations of state and costate at the time of closest approach after the manoeuvre are:

$$\delta\mathbf{b}_f = \mathbf{b}_f - \mathbf{b}_e, \quad (86)$$

$$\delta\boldsymbol{\lambda}_f = \boldsymbol{\lambda}_f. \quad (87)$$

The equations derived from the State Transition Matrix are now used to find another expression to link the initial costate  $\boldsymbol{\lambda}_0$  to the final position  $\mathbf{b}_f$ . From the first row of Eq. 85, it can be derived:

$$\delta\mathbf{b}_f = \boldsymbol{\Phi}_{12}\delta\boldsymbol{\lambda}_0 = \boldsymbol{\Phi}_{12}\boldsymbol{\lambda}_0 \quad (88)$$

and from Eq. 79:

$$\boldsymbol{\lambda}_0 = \nu 2\mathbf{C}^{-1}\mathbf{b}_f \quad (89)$$

Hence Eq. 88 can be rewritten as:

$$\delta\mathbf{b}_f = \nu\boldsymbol{\Phi}_{12}2\mathbf{C}^{-1}\mathbf{b}_f, \quad (90)$$

and exploiting the constraint on the squared Mahalanobis distance value (Eq. 78), the non-linear system in  $\nu$  and  $\mathbf{r}_f$  is obtained:

$$\begin{cases} \delta\mathbf{b}_f = \nu\boldsymbol{\Phi}_{12}2\mathbf{C}^{-1}\mathbf{b}_f \\ \text{SMD}(\mathbf{b}_f) = \overline{\text{SMD}} \end{cases} \quad \begin{cases} \mathbf{b}_f - \mathbf{b}_p = \nu\boldsymbol{\Phi}_{12}2\mathbf{C}^{-1}\mathbf{b}_f \\ \mathbf{b}_f^\top\mathbf{C}^{-1}\mathbf{b}_f = \overline{\text{SMD}}. \end{cases} \quad (91)$$

Manipulating the first equation of Eq. 91

$$\mathbf{b}_f(\mathbb{I}_{2 \times 2} - \nu\boldsymbol{\Phi}_{12}2\mathbf{C}^{-1}) = \mathbf{b}_p, \quad (92)$$

and plugging the expression for  $\mathbf{b}_f$  into the second equation, one obtains:

$$\begin{cases} \mathbf{b}_f = (\mathbb{I} - \nu\boldsymbol{\Phi}_{12}2\mathbf{C}^{-1})^{-1}\mathbf{b}_p \\ [(\mathbb{I} - \nu\boldsymbol{\Phi}_{12}2\mathbf{C}^{-1})^{-1}\mathbf{b}_p]^\top\mathbf{C}^{-1}(\mathbb{I} - \nu\boldsymbol{\Phi}_{12}2\mathbf{C}^{-1})^{-1}\mathbf{b}_p = \overline{\text{SMD}}. \end{cases} \quad (93)$$

Let us define  $\mathbf{F} = 2\boldsymbol{\Phi}_{12}\mathbf{C}^{-1}$  for easier notation and recall matrix  $\mathbf{Q} = \mathbf{C}^{-1}$ . The second equation of Eq. 93 becomes a scalar equation that can be solved for  $\nu$ :

$$[(\mathbb{I} - \nu\mathbf{F})^{-1}\mathbf{b}_p]^\top\mathbf{Q}(\mathbb{I} - \nu\mathbf{F})^{-1}\mathbf{b}_p = \overline{\text{SMD}}. \quad (94)$$

Since:

$$(\mathbb{I} - \nu\mathbf{F})^{-1} = \frac{1}{\det(\mathbb{I} - \nu\mathbf{F})} [\mathbb{I} - \nu\det\mathbf{F} \cdot (\mathbf{F})^{-1}] \rightarrow \quad (95)$$

$$\frac{1}{\det^2(\mathbb{I} - \nu\mathbf{F})} [(\mathbb{I} - \nu\det\mathbf{F} \cdot \mathbf{F}^{-1})\mathbf{b}_p]^\top\mathbf{Q}(\mathbb{I} - \nu\det\mathbf{F} \cdot \mathbf{F}^{-1})\mathbf{b}_p = \overline{\text{SMD}}. \quad (96)$$

Introducing also  $\tilde{\mathbf{F}} = \det\mathbf{F} \cdot \mathbf{F}^{-1}$ , and manipulating the equation through simple algebraic steps:

$$[(\mathbb{I} - \nu\tilde{\mathbf{F}})\mathbf{b}_p]^\top\mathbf{Q}(\mathbb{I} - \nu\tilde{\mathbf{F}})\mathbf{b}_p = \overline{\text{SMD}}\det^2(\mathbb{I} - \nu\mathbf{F}) \quad (97)$$

$$[\mathbf{b}_p^\top - \nu(\tilde{\mathbf{F}}\mathbf{b}_p)^\top]\mathbf{Q}[\mathbf{b}_p - \nu\tilde{\mathbf{F}}\mathbf{b}_p] = \overline{\text{SMD}}\det^2(\mathbb{I} - \nu\mathbf{F}) \quad (98)$$

$$\mathbf{b}_p^\top\mathbf{Q}\mathbf{b}_p - \nu\mathbf{b}_p^\top\mathbf{Q}\tilde{\mathbf{F}}\mathbf{b}_p - \nu(\tilde{\mathbf{F}}\mathbf{b}_p)^\top\mathbf{Q}\mathbf{b}_p + \nu^2(\tilde{\mathbf{F}}\mathbf{b}_p)^\top\mathbf{Q}(\tilde{\mathbf{F}}\mathbf{b}_p) = \overline{\text{SMD}}\det^2(\mathbb{I} - \nu\mathbf{F}) \quad (99)$$

The analytical equation is finally written in the normal polynomial form and can be solved in a closed-form for  $\nu$ :

$$\nu^2(\tilde{\mathbf{F}}\mathbf{b}_p)^\top\mathbf{Q}(\tilde{\mathbf{F}}\mathbf{b}_p) - \nu[\mathbf{b}_p^\top\mathbf{Q}\tilde{\mathbf{F}}\mathbf{b}_p + (\tilde{\mathbf{F}}\mathbf{b}_p)^\top\mathbf{Q}\mathbf{b}_p] = \overline{\text{SMD}}\det^2(\mathbb{I} - \nu\mathbf{F}) - \mathbf{b}_p^\top\mathbf{Q}\mathbf{b}_p. \quad (100)$$

In analogy with the final formula obtained with Cartesian dynamics, Eq. 100 has four solutions corresponding to the two local minima and two local maxima in terms of equivalent  $\Delta v$ .

The variation of the position reached after the manoeuvre in BP r.f.  $\mathbf{b}_f$  is found by plugging the solution  $\nu$  into the first equation of Eq. 93. Once  $\mathbf{b}_f$  is known, it is possible to compute  $\lambda_0$  from Eq. 89 and the IVP in Eq. 80, given all the initial conditions, can be integrated.

### 3.2.2. Miss distance constraint

The EOP in B-plane coordinates can be reformulated by constraining the final miss distance (MD) instead of the final PoC/SMD. Recalling the definition of miss distance in BP coordinates  $d = \sqrt{\xi_e^2 + \zeta_e^2} = \|\mathbf{b}_f\|$ , the non-linear system in Eq. 91 becomes:

$$\begin{cases} \delta \mathbf{b}_f = \nu \Phi_{12} 2\mathbf{C}^{-1} \mathbf{b}_f \\ d(\mathbf{b}_f) = \bar{d} \end{cases} \quad \begin{cases} \mathbf{b}_f - \mathbf{b}_p = \nu \Phi_{12} 2\mathbf{C}^{-1} \mathbf{b}_f \\ \|\mathbf{b}_f\| = \bar{d} \end{cases} \quad (101)$$

Manipulating the first equation of Eq. 101 and plugging  $\mathbf{b}_f$  into the second one:

$$\begin{cases} \mathbf{b}_f = (\mathbb{I}_{2 \times 2} - \nu \Phi_{12} 2\mathbf{C}^{-1})^{-1} \mathbf{b}_p \\ \left\| (\mathbb{I}_{2 \times 2} - \nu \Phi_{12} 2\mathbf{C}^{-1})^{-1} \mathbf{b}_p \right\| = \bar{d}. \end{cases} \quad (102)$$

and similarly to Eqs. 95 - 97:

$$\left\| \frac{1}{\det(\mathbb{I} - \nu \tilde{\mathbf{F}})} (\mathbb{I} - \nu \tilde{\mathbf{F}}) \mathbf{b}_p \right\| = \bar{d}. \quad (103)$$

In analogy to what has been explained for the squared Mahalanobis distance case, Eq. 103 is algebraically manipulated and analytically solved for  $\nu$  and used to find the initial costate and integrate the IVP in Eq. 80.

## 4. RESULTS

### 4.1. Test case

The methods presented are applied to a test case extracted from a large database of conjunction cases derived from the ESA Collision Avoidance Challenge [19] and then processed and collected in [20] and available for download. For the competition, ESA provided the teams with real conjunction data extracted from 162,634 CDM, corresponding to 13,154 unique events. These data were filtered to consider conjunctions with  $d \leq 2$  km and  $\text{PoC} > 10^{-6}$  resulting in a new data file with 2,170 conjunctions. All the conjunctions are relative to objects in LEO.

It is chosen to show the results considering a representative test case selected from the collision database. The method produces similar results for all conjunctions. A

representation of the selected test case can be found in Fig. 2 and Tab. 1 reports the position and velocity vectors of the primary and secondary spacecraft at conjunction in ECI frame, the collision probability PoC, the squared Mahalanobis distance SMD and the miss distance  $d$ . The combined cross-sectional radius of the spacecrafts is  $s_A = 29.7$  m.

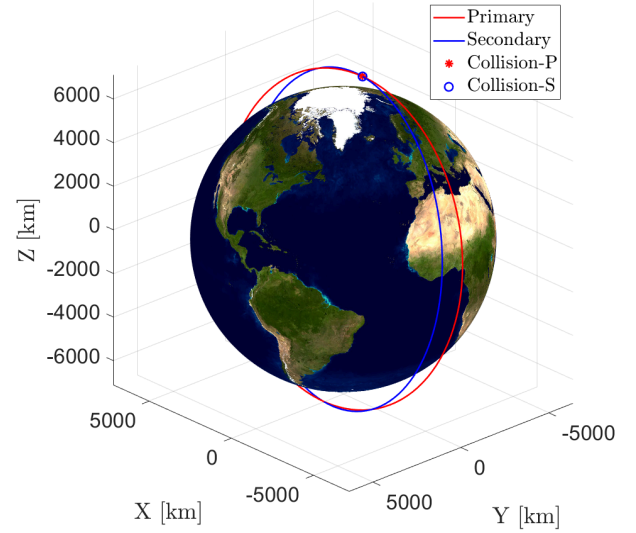


Figure 2. Test case collision representation.

Table 1. Test case conjunction data.

$\mathbf{r}_p$ [km]	$[2.3305, -1103.7, 7105.9]^T$
$\mathbf{r}_s$ [km]	$[2.3335, -1103.7, 7105.9]^T$
$\mathbf{v}_p$ [km/s]	$[-7.4429, -6.1373e-04, 3.9514e-03]^T$
$\mathbf{v}_s$ [km/s]	$[7.3537, -1.1428, -0.19825]^T$
PoC	1.3604e-01
SMD	0.87166
$d$ [km]	0.0432

The position uncertainties covariance matrices of the two satellites, expressed in their respective LVLH r.f., are:

$$\mathbf{C}_p = \begin{bmatrix} 0.9317 & -2.6234 & 0.2360 \\ -2.6234 & 1778.0 & -0.9331 \\ 0.2360 & -0.9331 & 0.1917 \end{bmatrix} \cdot 10^{-4} \text{ km}^2 \quad (104)$$

$$\mathbf{C}_s = \begin{bmatrix} 6.3466 & -19.6229 & 0.7077 \\ -19.6229 & 0.0820 & 11.3982 \\ 0.7077 & 11.3982 & 2.5103 \end{bmatrix} \cdot 10^{-4} \text{ km}^2 \quad (105)$$

The corresponding combined covariance matrix in B-plane coordinates is:

$$\mathbf{C} = \begin{bmatrix} 7.21756 & -0.7580 \\ -0.7580 & 51.9201 \end{bmatrix} \cdot 10^{-4} \text{ km}^2 \quad (106)$$

In the following subsections the methods with ECI and B-plane dynamics are validated and compared using a

dynamic model which only considers Keplerian motion. All the simulations presented are run on a Dell Inspiron 5593 with a processor 1.50 GHz Intel Core i7, 10th generation and 16 Gb Ram Memory.

#### 4.2. EOP in ECI coordinates

To illustrate the results of the proposed formulation and assess its accuracy, the optimal CAM is computed for each initial manoeuvring point in a range of 100 equally spaced values of true anomaly starting from 2 orbits before the TCA until the expected impact,  $\Delta\theta \in [0, 2 \cdot 2\pi]$ . The enforced value of squared Mahalanobis distance and the corresponding collision probability are:

$$\overline{\text{SMD}} = 25 \quad \rightarrow \quad \overline{\text{PoC}} = 2.4036 \cdot 10^{-6}. \quad (107)$$

The method described in Sec. 3.1 is applied, and after the control application the final position for each  $\Delta\theta$  is reported in BP r.f. in Fig. 3.

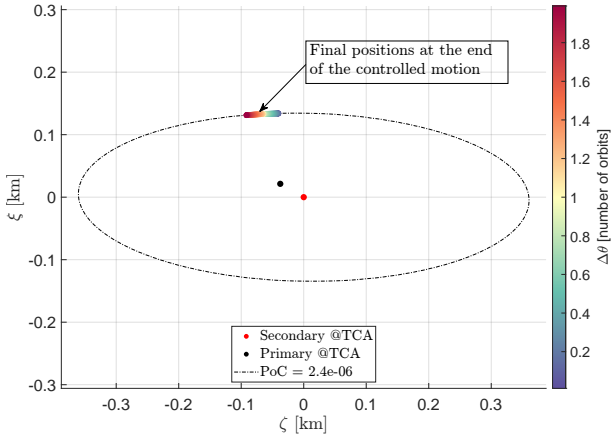


Figure 3. Final position in B-plane r.f. reached after the optimal CAM, for 100 initial manoeuvring points from 2 orbits before TCA until the expected impact. EOP with ECI dynamics and constrained SMD.

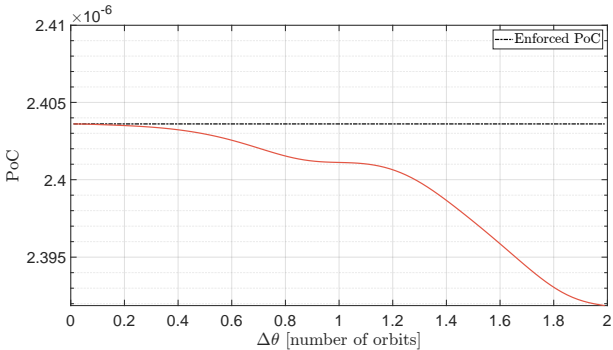


Figure 4. Collision probability profile after the dynamics propagation. EOP with ECI dynamics and constrained SMD.

The collision probability computed directly after the resolution of the system in Eq. 49 with the value of  $r_f$  resulting by Eq. 47 perfectly matches the enforced value (the maximum error is  $2.2371 \cdot 10^{-15}$ ). Then the actual final PoC is calculated with the final position  $r_f$  obtained after the integration of the manoeuvred dynamics in Eq. 34 and the resulting profile is shown in Fig. 4. The profile remains close to the threshold without ever exceeding it. The result is acceptable since at 2 orbits before the CA the maximum deviation is  $1.1729 \cdot 10^{-8}$ , two orders of magnitude lower than the constraint value.

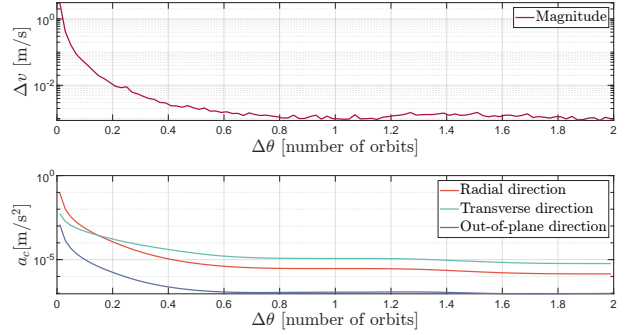


Figure 5. Equivalent impulse  $\Delta v$  (top) and maximum control acceleration  $a_c$  (bottom) for each initial manoeuvring point. EOP with ECI dynamics and constrained SMD.

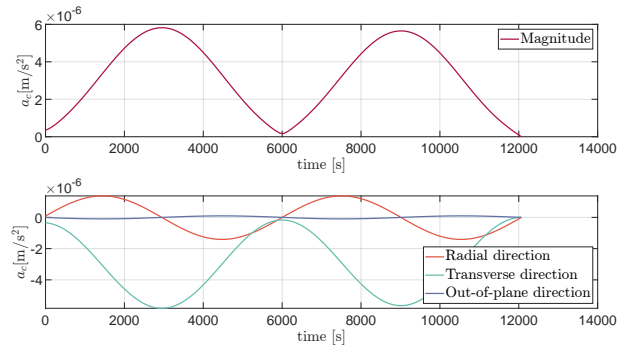


Figure 6. Control acceleration profile for a manoeuvre starting 2 orbits before TCA. EOP with ECI dynamics and constrained SMD.

After solving the optimal control problem, the control acceleration profile is found. For each  $\Delta\theta$  the equivalent cost in terms of  $\Delta v$  is calculated by integrating the acceleration profile and the resulting values are reported at the top of Fig. 5. The equivalent  $\Delta v$  increases consistently when the manoeuvre is performed close to the expected collision. The plot at the bottom of the same figure displays the trend of the maximum control acceleration required, with components in LVLH reference frame. Starting from the furthest points from the TCA, the transverse component dominates the others, but below a certain value of  $\Delta\theta$  close to CA the radial component becomes the largest. The profile of the control acceleration highly depends on which point is selected to start

the manoeuvre (value of  $\Delta\theta$ ). The results corresponding to a manoeuvre starting 2 orbits before TCA are shown in Fig. 6. The manoeuvre is mostly performed in the transverse direction. The maximum thrust required by the spacecraft and the necessary fuel mass can be seen in Fig. 7. The initial mass of the satellite is set to  $m_0 = 500$  kg and the specific impulse  $I_{sp} = 220$  s. As it can be noticed, the nearer to the collision point ( $\Delta\theta = 0$ ) the highest the mass required to match the constraint imposed on the collision probability.

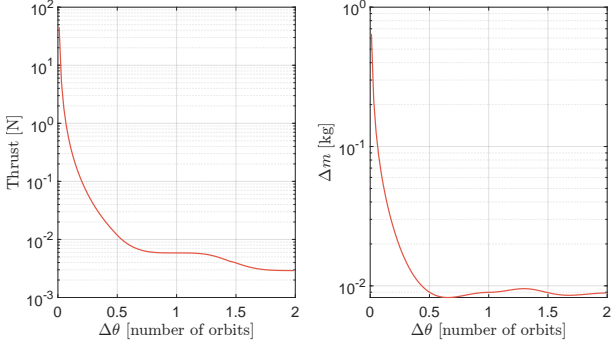


Figure 7. Maximum thrust (left) and mass variation (right) profile vs.  $\Delta\theta$  for EOP with ECI dynamics and constrained SMD.

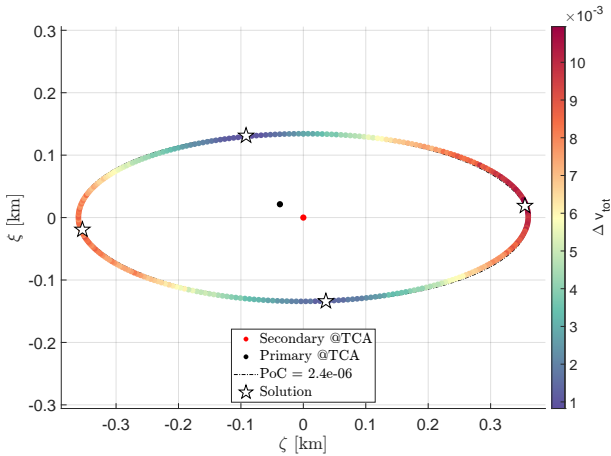


Figure 8. Solutions of EOP at 2 orbits before TCA compared with the  $\Delta v$  profile on the boundaries of the avoidance region.

As previously discussed, Eq. 61 has four solutions. A confirmation that those are two local maxima and two local minima in terms of total cost of the manoeuvre is achieved by the analysis of the objective function's behaviour on each point of the elliptical boundary. This analysis is done by sampling the ellipse of equal PoC with 300 points and solving optimal control problems where the final position is constrained to each specific point. Fig. 8 shows the results, where the stars indicates the four solutions of the equation. The examined cases have similar objective function structure, with the two minima located at the opposite side of the ellipse and corresponding

to thrust mainly aligned with either the tangential or the anti-tangential direction.

#### 4.2.1. Miss distance constraint

Considering miss distance constraint and setting  $\bar{d} = 0.3$  km, the final positions in B-plane coordinates after the controlled propagation are reported in Fig. 9. Similar to the previous case, the “estimated” miss distance (computed with  $r_f$  resulting from Eq. 65) perfectly matches the enforced value (maximum error:  $1.1347 \cdot 10^{-11}$  km). The actual final miss distance trend, calculated after the forward propagation, is displayed in Fig. 10; the profile remains close to the threshold without ever exceeding it, with a maximum deviation of  $1.1687 \cdot 10^{-4}$  km, three orders of magnitude lower than the constraint value.

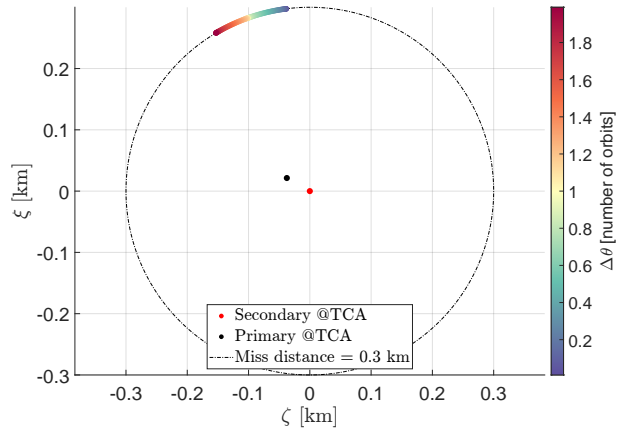


Figure 9. Final position in B-plane r.f. reached after the optimal CAM, for 100 manoeuvring points from 2 orbits before TCA until the expected impact. EOP with ECI dynamics and constrained MD.

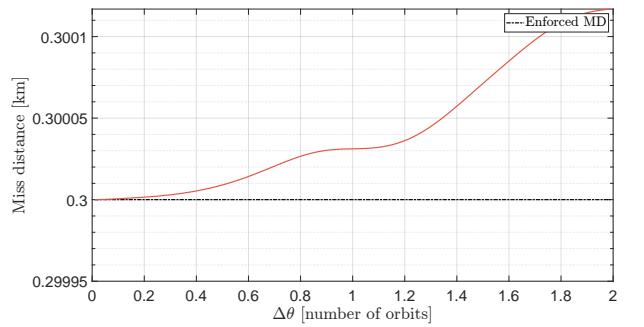


Figure 10. Miss distance profile after the dynamics propagation. EOP with ECI dynamics and constrained MD.

#### 4.3. EOP in B-plane coordinates

The results relative to the EOP formulation in BP dynamics are here reported. The same test case and the same

constraint values of Sec. 4.2 are considered. The method described in Sec. 3.2 is applied and, after the control application, the final positions for each  $\Delta\theta \in [0, 4\pi]$ , as expected, are almost indistinguishable from the ones reached exploiting ECI dynamics. The two solutions with ECI and BP dynamics are shown together on the same enlarged area of the B-plane in Fig. 11 and a better understanding can be achieved from the comparison of the trends of the final collision probability.

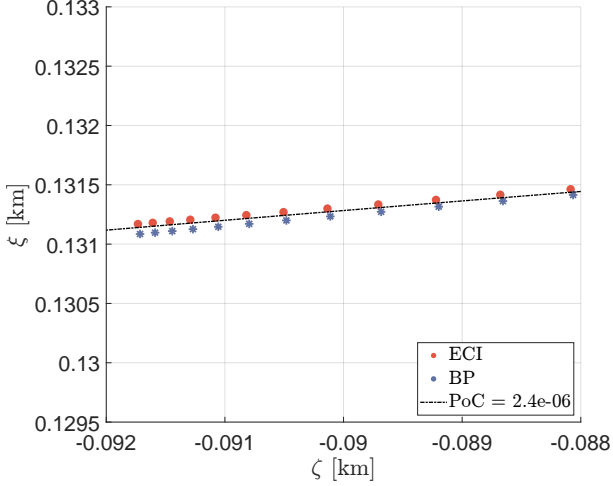


Figure 11. Final position in B-plane r.f. reached after the optimal CAM: comparison between EOP in ECI and BP coordinates, constrained SMD (detail of Fig. 3).

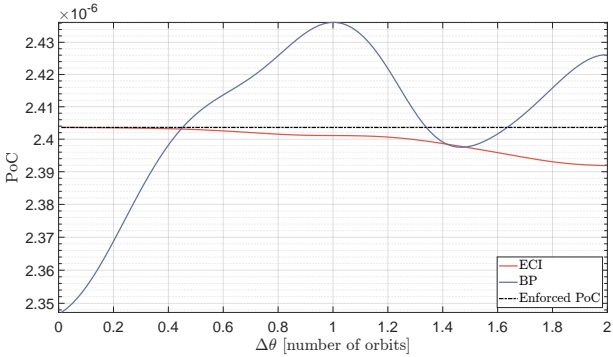


Figure 12. Collision probability profile after the dynamics propagation: comparison between EOP in ECI and BP coordinates, constrained SMD.

Fig. 12 shows the differences between ECI and BP dynamics in terms of final collision probability profile for each true anomaly of the initial manoeuvre point, calculated with the actual final position  $r_f/b_f$  obtained after the integration of the manoeuvred dynamics. Even though the ECI algorithm is more accurate and it never exceeds the threshold, both of them are close to the enforced value: for the B-plane algorithm the maximum deviation is  $5.6354 \cdot 10^{-8}$ , still in the same order of magnitude of the error with ECI coordinates, two order lower than the threshold.

#### 4.3.1. Miss distance constraint

The results of the EOP formulation with terminal function expressed in terms of miss distance are shown hereafter. As for the PoC/SMD case, the final position is nearly indistinguishable from the achieved with ECI dynamics formulation. Fig. 13 shows the final miss distance trend, computed through ECI and BP algorithm. The maximum deviation in the BP behaviour,  $3.3818 \cdot 10^{-4}$  km, is acceptable compared to the one in ECI r.f. of  $1.1687 \cdot 10^{-4}$  km, three order of magnitude lower the imposed value  $\bar{d} = 0.3$  km.

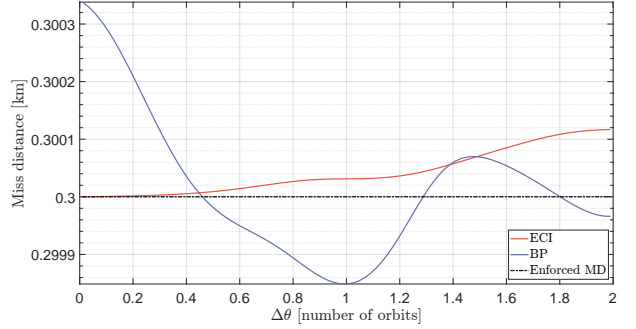


Figure 13. Miss distance profile after the dynamics propagation: comparison between EOP in ECI and BP coordinates, constrained MD.

#### 4.4. Perturbations effect

To test the accuracy of the EOP methods, a numerical propagation of the non-linear equations of motion is performed, using a more accurate dynamical model including environmental perturbations.

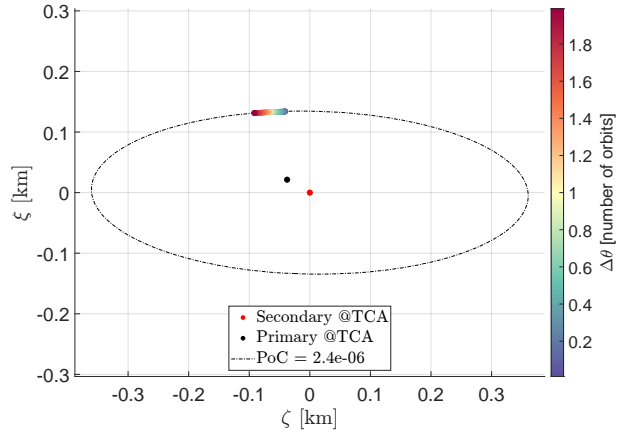


Figure 14. Final position in B-plane r.f. reached after the optimal CAM propagated with high fidelity model accounting for environmental perturbations; EOP in ECI coordinates with constrained SMD.

The same test case is adopted for the validation. Due to the fact that the collision occurs in LEO, the manoeuvre is

validated accounting for air drag perturbation (with coefficient  $c_D = 2.2$  and area-to-mass ratio equal to 0.3) and the first 10 Earth's gravitational harmonics. The algorithm presented in Sec. 3.1 is validated adjoining the perturbed dynamics: the problem in Eq. 34 is solved with the analytical solution, hence the control profile is retrieved with Keplerian dynamics and then it is applied and validated with a propagation using the more complete model. The final position reached after the propagation, for each initial point of the manoeuvre with  $\Delta\theta \in [0, 4\pi]$ , is reported in BP r.f. in Fig. 14. The results are almost indistinguishable from the ones reached exploiting the two-body problem dynamics (see Fig. 3). The two solutions with Keplerian and perturbed dynamics are shown together on the same enlarged area of the B-plane in Fig. 15 and a better understanding can be achieved from the comparison of the trends of the final collision probability.

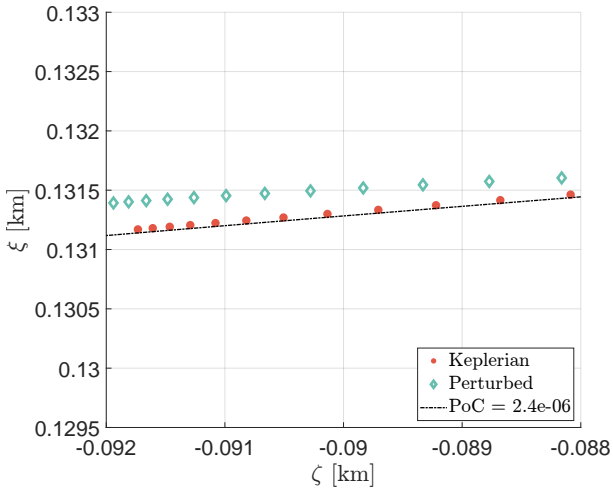


Figure 15. Final position in B-plane r.f. reached after the optimal CAM: comparison between Keplerian and perturbed dynamic model; EOP in ECI coordinates with constrained SMD. (Detail of Fig. 3 and Fig. 14).

Fig. 16 shows the differences between Keplerian and perturbed dynamics in terms of final collision probability profile for each true anomaly of the initial manoeuvre point, calculated with the actual final position  $\mathbf{r}_f$  obtained after the integration of the respective dynamics. Predictably, accounting for perturbations, the final collision probability deviates more from the enforced value with respect to Keplerian dynamics propagation, model in which the control is built. Nevertheless, the maximum deviation with disturbances is  $1.0531 \cdot 10^{-7}$ , a value that, compared to the two-body model error  $1.1729 \cdot 10^{-8}$ , is acceptable and still one order of magnitude lower than the threshold.

In conclusion, the variations introduced by atmospheric disturbances are minimal. Thus, they can be considered negligible for the optimal control problem presented, which turns out to be valid and accurate with the simple Keplerian orbit model.

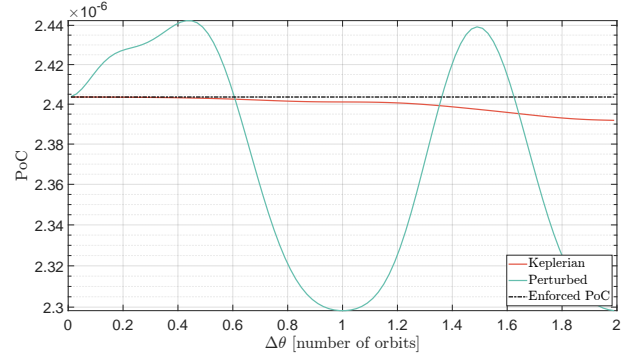


Figure 16. Collision probability profile after the dynamics propagation: comparison between Keplerian and perturbed dynamic model, EOP in ECI coordinates with constrained SMD.

#### 4.5. Computational Time

In this section the computational time (CT) of the method is analysed. The algorithms have been run on MATLAB<sup>®</sup> 2020a. Because the CT is of the order of fractions of second, to have results independent of the specific simulation conditions, every simulation is performed over 100 different collisions from the database and then averaged.

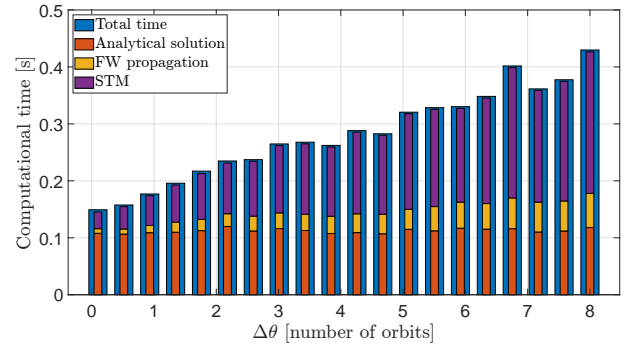


Figure 17. Computational time contributions of the EOP method with ECI dynamics and constrained SMD: time required to find the analytical solution from Eq. 61, time for the forward propagation and integration time of the STM.

The CT required for the EOP solution with ECI dynamics is plotted for  $\Delta\theta \in [0, 12\pi]$  in Fig. 17, showing the different contributions. In case of CAM performed close to the TCA, the integration time of the STM is low, but anticipating the manoeuvre, it becomes the main contribution.

Furthermore, consistently with the reduced dimension of the optimal control problem (the OCP in B-plane coordinates is has dimension two instead of six), the method with BP coordinates tends to be slightly faster than the algorithm with ECI dynamics.

The computational times obtained with MATLAB<sup>®</sup> are

in the order of magnitude of  $10^{-1}$  seconds: they promise good performances if implemented on-board.

## 5. CONCLUSIONS

A completely analytic solution for the energy-optimal control problem (EOP) was proposed for the optimal design of low-thrust collision avoidance manoeuvres (CAMs). Overall, the main assumptions of the proposed methods were constant and uncorrelated covariances, short-term encounters and spherical object approximation. The main conclusions are listed hereafter.

- Fully analytical solutions for continuous-thrust manoeuvre designs were proposed and validated, considering constraints in terms of final collision probability, squared Mahalanobis distance and miss distance.
- The EOP formulation projected into B-plane was found to be accurate and computationally more efficient than the algorithm in Cartesian coordinates, consistently with the reduction dimension of the optimal control problem from dimension six for the ECI formulation to dimension two.
- In the cases investigated, the optimal manoeuvres proved to be not too far from purely tangential manoeuvres in direction of the satellite's velocity.
- It was verified that environmental perturbations in LEO negligibly affect the accuracy of the method, therefore the manoeuvre design using the approximation of Keplerian dynamics is accurate.
- Finally, the computational times obtained with MATLAB<sup>®</sup> promise the feasibility of on-board implementation or massive calculation of CAMs.

The main limitations of the energy-optimal approach presented are the unbounded control in terms of thrust and acceleration and the non-optimal form in terms of propellant consumption. A possible future research activity could focus on transforming the unbounded acceleration profile into a bang-bang structure.

### A. APPENDIX: R, K, AND D MATRICES

$\mathbf{R}$  is the 2D rotation matrix:

$$\mathbf{R} = \begin{bmatrix} 0 & 0 & -1 \\ -\sin \beta & -\cos \beta & 0 \end{bmatrix}$$

where the angle  $\beta$  can be expressed as:

$$\cos \beta = \frac{1 - \chi \cos \psi \cos \phi}{\sqrt{1 - 2\chi \cos \psi \cos \phi + \chi^2}}$$

$$\sin \beta = \sqrt{1 - \cos^2 \beta}$$

and:

$$\phi = \text{atan2}[(\mathbf{v}_p \times \mathbf{v}_s) \cdot \mathbf{u}_{h1}, \mathbf{v}_p \cdot \mathbf{v}_s]$$

$$\psi = \tan^{-1} \left[ \frac{(\mathbf{v}_s \cdot \mathbf{u}_{h1}) \|\mathbf{v}_s \times \mathbf{u}_{h1}\|}{v_s^2 - (\mathbf{v}_s \cdot \mathbf{u}_{h1})^2} \right]$$

$$\chi = \frac{v_s}{v_p}.$$

where  $\mathbf{u}_{h1}$  is the normal of  $O_p$  orbital plane. The kinematics matrix  $\mathbf{K}$  reads:

$$\mathbf{K} = \begin{bmatrix} -v_p \sqrt{\frac{R_c}{\mu}} & \sin \alpha_c & 0 \\ 0 & -\frac{\cos \alpha_c \sin \phi \cos \psi}{\sqrt{1 - \cos^2 \psi \cos^2 \phi}} & \frac{\sin \psi}{\sqrt{1 - \cos^2 \psi \cos^2 \phi}} \\ 0 & \frac{\cos \alpha_c \sin \psi}{\sqrt{1 - \cos^2 \psi \cos^2 \phi}} & \frac{\sin \phi \cos \psi}{\sqrt{1 - \cos^2 \psi \cos^2 \phi}} \end{bmatrix}$$

where  $\alpha_c$  is the flight path angle of  $O_p$  at the TCA which obeys:

$$\sin \alpha_c = \frac{e_0 \sin \theta_c}{\sqrt{e_0^2 + 2e_0 \cos \theta_c + 1}},$$

$$\cos \alpha_c = \frac{1 + e_0 \cos \theta_c}{\sqrt{e_0^2 + 2e_0 \cos \theta_c + 1}}.$$

The dynamics matrix  $\mathbf{D}$  reads:

$$\mathbf{D} = \sqrt{\frac{R_c^3}{\mu}} \begin{bmatrix} d_{tr} & d_{t\theta} & 0 \\ d_{rr} & d_{r\theta} & 0 \\ 0 & 0 & d_{wh} \end{bmatrix}$$

where  $d_{tr}, d_{t\theta}, d_{rr}, d_{r\theta}$  and  $d_{wh}$  are non-dimensional functions of time that can be derived using the generalised Pelaez' orbital elements (see [21]) of the initial  $O_p$  orbit:

$$q_{10} = \frac{e_0}{\sqrt{1 + e_0 \cos \theta_c}},$$

$$q_{30} = \frac{1}{\sqrt{1 + e_0 \cos \theta_c}}.$$

$$d_{rr} = \frac{\sin(\theta_c - \theta)}{q_{30}(q_{30} + q_{10} \cos \theta_c)^2},$$

$$d_{r\theta} = \frac{2q_{30}(1 - \cos((\theta_c - \theta))) - q_{10} \sin \theta \sin(\theta_c - \theta)}{q_{30}(q_{30} + q_{10} \cos \theta)(q_{30} + q_{10} \cos \theta_c)^2},$$

$$d_{wh} = \frac{\sqrt{q_{30}^2 + q_{10}q_{30} \cos \theta_c}}{q_{30} + q_{10} \cos \theta} \sin(\theta_c - \theta),$$

$$d_{tr} = \frac{1}{q_{30}(q_{30}^2 - q_{10}^2)^2(q_{30} - q_{10} \cos E)}$$

$$\times [e_{r1}(E_c - E) + e_{r2}(\sin E_c - \sin E)$$

$$+ e_{r3}(\sin 2E_c - \sin 2E) + e_{r4}(\cos E_c - \cos E)$$

$$+ e_{r5}(\cos 2E_c - \cos 2E)],$$

$$d_{t\theta} = \frac{1}{q_{30}(q_{30}^2 - q_{10}^2)^{5/2}(q_{30} - q_{10} \cos E)}$$

$$\times [e_{\theta1}(E_c - E) + e_{\theta2}(\sin E_c - \sin E)]$$

$$+ e_{\theta 3}(\sin 2E_c - \sin 2E) + e_{\theta 4}(\cos E_c - \cos E) \\ + e_{\theta 5}(\cos 2E_c - \cos 2E)],$$

where:

$$e_{\theta 1} = 3q_{30}(q_{30}^2 - q_{10}^2), \\ e_{\theta 2} = \frac{1}{2}[3q_{10}^3 - (2q_{30}^2 - q_{10}^2)(4q_{30} \cos E - q_{10} \cos 2E)], \\ e_{\theta 3} = \frac{q_{10}q_{30}}{4}[4q_{30} \cos E - q_{10}(3 + \cos 2E)], \\ e_{\theta 4} = q_{30}[(4q_{30}^2 - 2q_{10}^2) \sin E - q_{10}q_{30} \sin 2E], \\ e_{\theta 5} = -\frac{q_{10}}{4}[(4q_{30}^2 - 2q_{10}^2) \sin E - q_{10}q_{30} \sin 2E], \\ e_{r1} = 3q_{10}q_{30} \sin E, \\ e_{r2} = -2(q_{30}^2 + q_{10}^2) \sin E, \\ e_{r3} = \frac{q_{10}q_{30}}{2} \sin E, \\ e_{r4} = -2q_{30}(q_{30} \cos E - q_{10}), \\ e_{r5} = \frac{q_{10}}{2}(q_{30} \cos E - q_{10}).$$

where  $E_c$  and  $E$  are the eccentric anomalies corresponding to  $\theta_c$  and  $\theta$  respectively, and accounting for multiple revolutions.

## REFERENCES

1. ESA. *Safety & Security, Space Debris* [https://www.esa.int/Safety\\_Security/Space\\_Debris/](https://www.esa.int/Safety_Security/Space_Debris/)
2. Flohrer, T. & Krag, H. *Space surveillance and tracking in ESA's SSA programme in Proceedings 7th European Conference on Space Debris, Darmstadt, Germany* (2017).
3. Merz, K. *et al. Current collision avoidance service by esa's space debris office in 7th European Conference on Space Debris, Darmstadt, Germany* (2017), 18–21.
4. Bombardelli, C. & Hernando-Ayuso, J. Optimal impulsive collision avoidance in low earth orbit. *Journal of Guidance, Control, and Dynamics* **38**, 217–225 (2015).
5. Bombardelli, C. Analytical formulation of impulsive collision avoidance dynamics. *Celestial Mechanics and Dynamical Astronomy* **118**, 99–114 (2014).
6. Bombardelli, C., Hernando-Ayuso, J. & Garcia-Pelayo, R. Collision avoidance maneuver optimization. *Advances in the Astronautical Sciences* **152**, 1857–1870 (2014).
7. Morselli, A., Armellin, R., Di Lizia, P. & Bernelli-Zazzera, F. Collision avoidance maneuver design based on multi-objective optimization. *Advances in the Astronautical Sciences* **152**, 1819–1838 (2014).
8. Reiter, J. A. & Spencer, D. B. Solutions to rapid collision-avoidance maneuvers constrained by mission performance requirements. *Journal of Spacecraft and Rockets* **55**, 1040–1048 (2018).
9. Salemme, G., Di Lizia, P. & Armellin, R. *Continuous-thrust collision avoidance manoeuvres optimization in AIAA Scitech 2020 Forum* (2020).
10. Schiavo, A. *Numerically efficient design of low-thrust collision avoidance manoeuvre* MA thesis (School of industrial, information engineering, Department of aerospace science, and technology, Politecnico di Milano, Italy, 2020).
11. Gonzalo Gomez, J., Colombo, C. & Di Lizia, P. *A semi-analytical approach to low-thrust collision avoidance manoeuvre design in 70th International Astronautical Congress (IAC 2019)* (2019), 1–9.
12. Hernando-Ayuso, J. & Bombardelli, C. Low-Thrust Collision Avoidance in Circular Orbits. *Journal of Guidance, Control, and Dynamics*, 1–13 (2021).
13. Belmonte Hernandez, C., Martínez Chamarro, Á. & Armellin, R. Low-Thrust Collision Avoidance Maneuvers using Optimal Control Theory and Convex Optimization. *31st Space Flight Mechanics Meeting* (2021).
14. Armellin, R. *Collision Avoidance Maneuver Optimization with a Multiple-Impulse Convex Formulation 2021*. arXiv: 2101.07403 [math.OC].
15. Chan, F. K. *et al. Spacecraft collision probability* (Aerospace Press El Segundo, CA, 2008).
16. Valsecchi, G. B., Milani, A., Gronchi, G. F. & Chesley, S. R. Resonant returns to close approaches: Analytical theory. *Astronomy & Astrophysics* **408**, 1179–1196 (2003).
17. Montaruli, M. F. *Collision risk assessment and collision avoidance maneuver planning* MA thesis (Politecnico di Milano, Italy, 2019).
18. Bryson, A. E. *Applied optimal control: optimization, estimation and control* 47–55 (CRC Press, 1975).
19. ESA. *Collision Avoidance Challenge*, <https://kelvins.esa.int/collision-avoidance-challenge/data/>
20. Armellin, R. *Github*, <https://github.com/arma1978/conjunction/>
21. Pelàez, J., Hedo, J. M. & de Andrès, P. R. A special perturbation method in orbital dynamics. *Celestial Mechanics and Dynamical Astronomy* **97**, 131–150 (2007).